

Cite this: *Mater. Adv.*, 2023,
4, 3473

The parameter space for scalable integration of atomically thin graphene with Nafion for proton exchange membrane (PEM) applications

Pavan Chaturvedi,^{†a} Nicole K. Moehring,^{†abc} Thomas Knight,^d Rahul Shah,^{bc}
Ivan Vlasiouk^e and Piran R. Kidambi^{ib*abcef}

Selective proton permeation through atomically thin graphene while maintaining impermeability to even small gas atoms *i.e.* He or hydrated ions, presents potential for advancing proton exchange membranes (PEMs) across a range of energy conversion and storage applications. The incorporation of graphene into state-of-the-art proton conducting polymers *e.g.* Nafion can enable improvements in PEM selectivity as well as mitigate reactant crossover. The development of facile integration approaches are hence imperative. Here, we systematically study the parameters influencing the integration of monolayer graphene synthesized *via* scalable chemical vapor deposition (CVD) on polycrystalline Cu foils with a model proton conducting polymer (Nafion) *via* a facile hot-press process. The hot-press time (*t*), temperature (*T*) and pressure (*P*) are found to not only influence the quality of graphene transfer but can also introduce additional defects in the CVD graphene. Graphene transfers to Nafion performed below the optimum temperature ($T_{\text{opt}} \sim 115$ °C) remain patchy with ruptures, while transfers above T_{opt} showed defect features, and transfers near T_{opt} show minimal ruptures and defect features. We demonstrate Nafion|graphene|Nafion sandwich membranes using the optimal transfer conditions that allow for $\sim 50\%$ reduction in hydrogen crossover (~ 0.17 mA cm⁻²) in comparison to Nafion control membranes (~ 0.33 mA cm⁻²) while maintaining comparable proton area specific resistance < 0.25 Ω cm² (areal conductance $\sim 4\text{--}5$ S cm⁻²), that are adequate to enable practical PEM applications such as fuel cells, redox flow batteries, and beyond.

Received 19th April 2023,
Accepted 3rd July 2023

DOI: 10.1039/d3ma00180f

rsc.li/materials-advances

Introduction

Selective proton transport through the atomically thin lattice of pristine graphene in combination with its impermeability to gases and hydrated ions has ignited research interest in advancing proton exchange membranes for a range of energy generation and conversion processes including fuel cells, redox flow batteries, electrolyzers *etc.*^{1–15} The industry standard state-of-the-art proton-selective, polymeric membrane - Nafion exhibits proton

conductance > 1 S cm⁻², but suffers from persistent issues of reactant crossover (diffusion/transport of undesired species), which decreases the energy efficiency of devices, particularly over long-term operations.¹

In this context, pristine atomically thin monolayer graphene (obtained *via* mechanical exfoliation from graphite) has been shown to be impermeable to even small atoms such as He, but allows for proton permeation.³ However, areal proton conductance of pristine graphene ~ 3 mS cm⁻² over micron-scale areas³ is too low for practical applications. Graphene grown *via* chemical vapor deposition (CVD) on the other hand also exhibits proton conductance of ~ 5 mS cm⁻² over micron-scale areas,¹⁶ but centimeter-scale CVD graphene shows much higher proton conductance > 1 S cm⁻² due to presence of intrinsic defects.^{10,16–18} The ability to precisely control intrinsic defects in CVD graphene^{18–21} *via* bottom-up synthesis presents potential for advancing PEMs by mitigating persistent issues of reactant crossover *via* steric hinderance to transport of atoms and hydrated ions while allowing enhanced proton permeation through defects.^{18,22}

A facile and scalable approach is to incorporate an atomically thin layer of monolayer CVD graphene with precisely

^a Chemical and Biomolecular Engineering Department, Vanderbilt University, Nashville, TN, 37212, USA. E-mail: piran.kidambi@vanderbilt.edu^b Interdisciplinary Graduate Program in Materials Science, Vanderbilt University, Nashville, TN, 37235, USA^c Vanderbilt Institute of Nanoscale Science and Engineering, Nashville, TN, 37212, USA^d Department of Chemistry, Vanderbilt University, Nashville, TN, 37235, USA^e Center for Nanophase Materials Sciences, Oak Ridge National Laboratory, Oak Ridge, TN, USA^f Mechanical Engineering Department, Vanderbilt University, Nashville, TN, 37212, USA[†] These authors contributed equally.

controlled intrinsic defects with Nafion to mitigate crossover issues prevalent in polymeric proton exchange membranes while simultaneously maintaining high proton transport (area specific resistance $<1 \Omega \text{ cm}^2$ or conductance $>1 \text{ S cm}^{-2}$) for practical PEM applications.¹ Here, the development of a scalable integration approach with minimal processing steps, allowing direct transfer of graphene from the growth substrate to Nafion without the use of any sacrificial supports or accompanying residues is imperative.^{23,24} Conformal contact between CVD graphene synthesized on polycrystalline Cu foils and the Nafion (by leveraging the glass transition temperature T_g),^{23,25,26} minimal damage to the graphene and scalability of the processes are also highly desirable for direct graphene transfer to proton conducting polymer substrates for PEM applications.^{23,25,26} Some studies have shown that hot-pressing allows for graphene transfer to Nafion for applications in fuel cells,⁷ as well as isotope separation,^{9,10,27} where in the conditions of transfer significantly influence performance.^{28,29}

Here, we systematically probe parameters affecting facile and scalable transfer of CVD graphene to Nafion *via* hot-press.^{18,22}

We find the parameters such as time (t), temperature (T) and pressure (P) significantly influence the quality of direct transfer of CVD graphene to Nafion. We demonstrate Nafion|graphene|Nafion sandwich membranes with $\sim 50\%$ reduction in hydrogen crossover in comparison to the Nafion sandwich (Nafion||Nafion) control membrane while maintaining adequate proton area specific resistance (ASR) $< 0.25 \Omega \text{ cm}^2$ (areal conductance $\sim 4\text{--}5 \text{ S cm}^{-2}$) for practical PEM applications.

Experimental

Graphene synthesis

Graphene synthesis on polycrystalline Cu foils (thickness $\sim 65 \mu\text{m}$) was performed *via* chemical vapor deposition at atmospheric pressure using methane and hydrogen gases at $>1000 \text{ }^\circ\text{C}$ as described in detail elsewhere.^{30–32}

Scanning electron microscopy

The surface morphology of CVD graphene on Cu as well as after transferring to Nafion was imaged using a Zeiss Merlin scanning electron microscope (SEM) at an acceleration voltage of $\sim 2 \text{ kV}$.

Raman spectroscopy

Raman spectra were measured using a Thermo Scientific DXR confocal Raman microscope equipped with a 534 nm laser and a grating of 900 lines per mm (resolution $5.5\text{--}8.3 \text{ cm}^{-1}$), $\sim 1 \text{ mW}$ laser power and a spot size of $\sim 1.1 \mu\text{m}$.

CVD graphene was transferred from Cu substrate to 300 nm SiO_2/Si wafer substrates using a poly (methyl methacrylate) carrier layer. The Cu was etched in ammonium persulfate (APS) solution followed by rinses in DI water. PMMA was removed using acetone followed by iso-propanol as described in detail elsewhere.^{16,18,19,21,33–36}

Acid etch test and analysis

The etch test was performed by placing $\sim 10 \mu\text{l}$ of 0.1 M FeCl_3 on CVD graphene|Cu for 5 s followed by two water washes as described in detail elsewhere.^{16,18,37} The CVD graphene|Cu is then dried in ambient conditions and imaged under SEM to identify etch pits. Etch pits appear as bright spots in the SEM images and serve as an indication of defects in the graphene through which the acid permeates and etches pits in Cu.^{16,18,37}

Differential scanning calorimetry (DSC)

DSC measurements were performed using STA-1000 (Instrument specialists incorporated) at a ramp rate of $\sim 10 \text{ }^\circ\text{C min}^{-1}$ under an Argon environment. $\sim 11.639 \text{ mg}$ of as received H-form Nafion (N211 procured from Ion Power, thickness $\sim 25.4 \mu\text{m}$) and N211 hot-pressed at $115 \text{ }^\circ\text{C}$ for 45 s at 200 psi ($\sim 10.244 \text{ mg}$) were used to probe the glass transition temperature range and potential influence of water content/hot pressing.

Transfer of graphene to Nafion *via* hot-press

The transfer of graphene on Nafion was performed *via* hot-press.^{2,10,11,16–18} Briefly, a graphene|Cu piece was placed on Nafion 211 (N211, $\sim 25.4 \mu\text{m}$ thickness, Ion Power), and sandwiched between two PTFE coated fiber glass sheets and hot-pressed (see schematic in Fig. 1D). Temperature is controlled *via* thermocouples in the heated platens of the hot press. We used hot-press times of 120 s and 45 s, pressures of 200 psi and 1000 psi and temperatures of $95\text{--}140 \text{ }^\circ\text{C}$. The optimum hot-press condition for graphene transfer to N211 corresponds to $T_{\text{opt}} \sim 115 \text{ }^\circ\text{C}$, $t = 45 \text{ s}$, and $P \sim 200 \text{ psi}$.

After the hot-press, the PTFE fiber sheet in the bottom side is carefully removed without disturbing the pressed graphene|Cu to obtain a PTFE|N211|graphene|Cu stack which is floated on 0.2 M APS solution to etch the Cu. After complete etching of Cu, the stack is floated on two separate DI water baths for 15 minutes each and dried under ambient conditions. The obtained N211|graphene was used for characterization of surface morphology of graphene transferred to N211 *via* SEM. Analysis (*via* thresholding using ImageJ software³⁸) of spot like defects (formed likely *via* oxidation of Cu underneath defects in graphene) was performed on the Cu|graphene|Nafion stack. After Cu etching, the N211|graphene was pressed at $\sim 115 \text{ }^\circ\text{C}$, $\sim 200 \text{ psi}$ for 45 s against a second piece of N211 to prepare a sandwich Nafion|graphene|Nafion membrane. The sandwich membranes were soaked in 0.1 M HCl for 24 hours before testing. We note the actual temperature of the N211 during hot-pressing could be lower than the set temperature of the platens due to the presence of the Teflon sheets.

Measurement of proton transport

The N211|graphene|N211 sandwich membrane was used to measure proton transport as described in detail elsewhere.¹⁸ Pt/C (Pt loading 0.2 mg cm^{-2} , fuel cell store) electrodes were used as anode and cathode and were hot-pressed at $140 \text{ }^\circ\text{C}$ for 1 min at 400 psi to the Nafion|graphene|Nafion sandwich



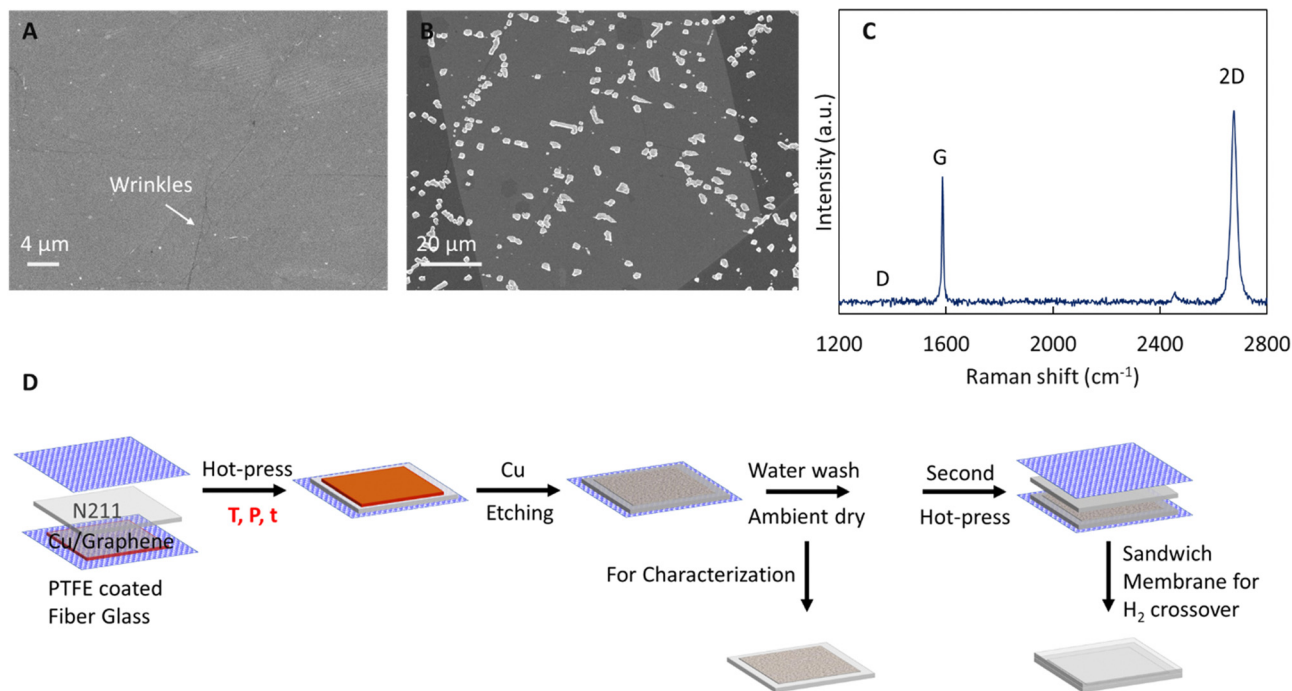


Fig. 1 SEM image of (A) as synthesized graphene on Cu foil, and (B) etch pits on graphene|Cu after 5 s acid etch test with 0.1 M FeCl₃. (C) Raman spectrum of graphene transferred onto 300 nm SiO₂/Si substrate and (D) schematic of graphene transfer process to Nafion (N211).

membrane. The areal resistance was measured while supplying humidified H₂ gas to both sides of the membrane *via* linear sweep voltammetry (LSV). The slope of the resulting *I*-*V* curve is equivalent to the membrane areal proton conductance and the inverse equal to the area specific resistance (ASR, after normalizing current to electrode area, ~0.32 cm²). To measure the H₂ crossover, the gas environment was changed to H₂ and N₂ on opposite sides of the membrane. The diffused H₂ was measured as an oxidation current which is a measure of crossover across the membranes. The crossover current was reported at 0.4 V measured in 100% humidity at room temperature.

Results and discussions

We initially assess the quality of the as synthesized monolayer graphene on Cu (see SEM image in Fig. 1A with wrinkles confirming graphene) *via* acid etch test (Fig. 1B) and Raman spectroscopy (Fig. 1C) after transfer to 300 nm SiO₂/Si wafer. In acid etch test, FeCl₃ permeates through defects in graphene and reacts with the underlying Cu substrate forming etch pits in the Cu foil which can be imaged with SEM to provide an indication of graphene quality.¹⁰ The total etched area of ~7% is comparable to other prior reports for high quality graphene and the etch pits predominately seem to occur along wrinkles in the graphene.^{10,16,18,39} Next, Raman spectroscopy is used to probe the high crystalline quality of the synthesized graphene. The Raman spectra (Fig. 1C) shows the characteristic 2D (~2700 cm⁻¹) and G (~1580 cm⁻¹) peaks, an absence of the D-peak (~1350 cm⁻¹), $I_{2D}/I_G > 1$, and 2D peak

full width at half maxima (FWHM) < 30 cm⁻¹, confirming high quality of the synthesized monolayer CVD graphene.^{40,41}

Having confirmed the high crystalline quality of the graphene, we proceed to systematically study parameters (see Table 1) influencing the transfer of graphene to a model proton conducting polymer Nafion (N211). We select hot-press as a facile and scalable process to achieve direct transfer of graphene to Nafion without the use of carrier layers and associated residues,^{21,34,36} and probe the influence of hot-press (i) time (*t*), (ii) temperature (*T*), and (iii) pressure (*P*).

Initially, we probe the effect of hot-press time on graphene transfer to N211 and transfer graphene at hot-press conditions of 140 °C and 200 psi for two different hot-press times of 120 s and 45 s, as shown in Fig. 2A and B, respectively. Our rationale for choosing the highest temperature of hot-press ~140 °C and the lowest pressure ~200 psi in our study for the time dependence is to allow for clear observations by exacerbating effects that might not occur at lower temperatures as discussed further below. Optical microscopy images of the Cu|graphene|N211 surface shows dark spots (shown *via* arrows) for both conditions. However, with shorter hot-press time (45 s) the computed area of dark spots is significantly lower than 120 s (Fig. 2 and Table 1). The dark spots appear isolated for 45 s (Fig. 2A) in comparison to 120 s where the dark spots appear to coalesce into line like features (Fig. 2B and Table 1). ImageJ analysis of the % area of the dark spots are ~0.5% for 45 s and ~4% for 120 s, as shown in Fig. 2C, confirming longer press time results in higher dark spot like features. The density of the spots in Fig. 2B appear to be similar to the density of etch pits (Fig. 1B) and they also occur predominantly along wrinkles, as



Table 1 Summary of parameters studied for CVD graphene transfer to Nafion (N211)

Temperature (°C)	Pressure (psi)	Time (s)	Defects features		Observations
			Ruptures	Spot like defects	
140	600	120	Optical images showed spot like defect features.		Spot like defect features observed appear similar to etch pit formed upon acid etch of graphene on Cu, suggesting oxidation of Cu underneath defects in graphene causes further damage to graphene.
140	600	45	Clustering of these spots appear similar to line like features or cracks in graphene and represent an intermediate between ruptures and spots.		
140	200	120	Optical images showed spot like defect features.		Spot like defect features seen in optical images. Not shown here. Temperature series for optimal $t = 45$ s is shown in Fig. 3 and analysis shown below within Table 1.
130	200	120	Clustering of these spots appear similar to line like features or cracks in graphene and represent an intermediate between ruptures and spots. No statistical difference seen in spot like defect features in optical images.		
120	200	120	Large patches of missing graphene layer (ruptures) observed.		
90	200	120	Large patches of missing graphene layer (ruptures) observed.	Almost no spot like defect features observed.	SEM images showed large (several μm^2) of missing graphene area in the form of large patches in the film (ruptures). Not shown here.
50	200	120			
140	200	45	$4.49 \pm 2.75\%$	$0.14 \pm 0.35\%$	Analysis of SEM images is used to estimate area % of defects. Lower temperatures ($< T_{\text{opt}}$) results in ruptures whereas high temperatures ($> T_{\text{opt}}$) result in spot like defect features.
115	200	45	$0.38 \pm 0.28\%$	$0.27 \pm 0.09\%$	
110	200	45	$0.22 \pm 0.09\%$	$2.27 \pm 1.39\%$	
90	200	45	$0.43 \pm 0.19\%$	$2.57 \pm 0.11\%$	

also observed for the acid etch test, suggesting these features originate from Cu oxidation underneath defects in CVD graphene on Cu foil. Hence, we propose oxidation of Cu underneath the graphene at elevated temperatures as a potential source for these dark spots. Such oxidation of Cu results in damage/holes in the CVD graphene and can also lead to poor transfer to Nafion due to non-uniformity of the surface.

Hence, we select 45 s as the duration of hot-press, $P = 200$ psi, and proceed to probe the influence of temperature on the quality of graphene transfer to Nafion. We specifically choose temperatures near the range of T_g values for Nafion in literature.^{42–44} In addition to optical microscopy images of Cu|graphene|N211 (Fig. 2A and B) we also used SEM to probe the surface morphology of the graphene transferred onto N211. Fig. 3A shows an SEM image of graphene transferred onto Nafion at $T \sim 140$ °C with damages to graphene, specifically spot like defect features as well as clusters of spots resembling line like features.

Although the overall transfer yield appears high with minimal patches of missing graphene, there appear to be features consistent with damage to the graphene film or defects (shown

by arrows) covering $\sim 5\%$ of the total area. The defect features resemble the shape and density of the dark spots observed in optical images shown in Fig. 2, confirming that the observed dark spots correspond to damage to the graphene transferred to N211 (Fig. 3A) and stem from oxidation of Cu underneath defects in graphene on Cu consistent with Fig. 2.

To mitigate the dark spots a series of transfers were performed at lower temperatures while keeping hot-press time ~ 45 s and $P \sim 200$ psi. Interestingly, upon lowering the temperature to $T \sim 115$ °C (referred to as T_{opt}) *i.e.* $T \sim T_{\text{opt}}$, the dark spot like defects account for $< 1\%$ of the defective area (Fig. 3B). However, at lower temperatures $T < T_{\text{opt}}$ we also observe macroscopic ruptures in the graphene (Fig. 3C and Table 1). These ruptures are identified in SEM images as holes in graphene with bi-layer graphene regions around the edges. The ruptures originate from the apparent lack of adhesion of graphene to Nafion, which ‘flips over’ to form a bi-layer graphene area around the edges. With decreasing temperature, the percent area due to these ruptures increases up to $\sim 3\%$ at 90 °C (Fig. 3D and Table 1). Since these features are not observed at temperatures above the T_{opt} , we suspect they

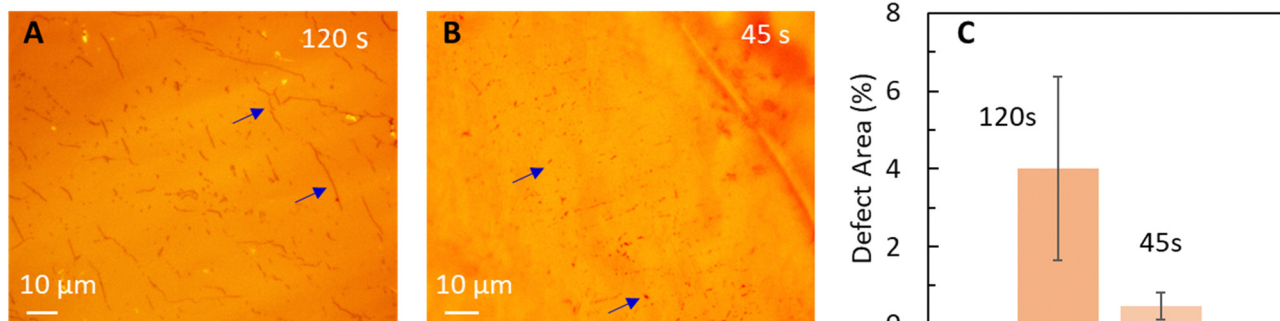


Fig. 2 Optical images of graphene transferred to Nafion (N211) via hot-press (~ 140 °C, ~ 200 psi) for (A) 120 s, and (B) 45 s. Blue arrows indicate spot like defects that correspond to damages in graphene via oxidation of Cu. Hot-press for longer duration leads to line like larger features (A and Table 1) corresponding to Cu oxidation and damage to graphene. (C) Comparison of % defect area for different hot-press times.



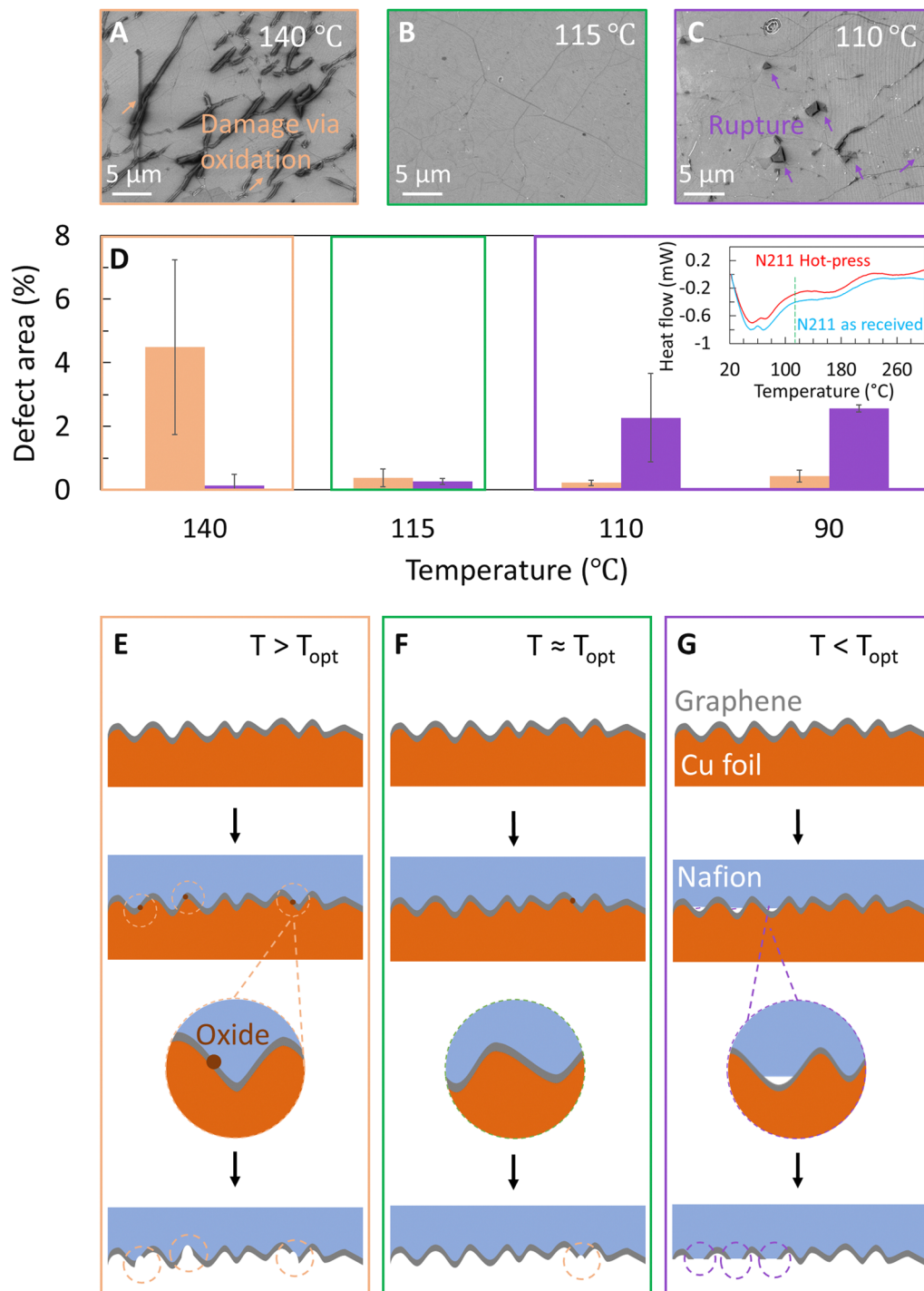


Fig. 3 SEM images of graphene transferred to Nafion 211 at (A) 140 °C ($> T_{\text{opt}}$), (B) 115 °C ($\sim T_{\text{opt}}$) and (C) 110 °C ($< T_{\text{opt}}$). At higher temperatures, spot like features similar to damage to graphene on Cu foil via oxidation of Cu underneath defects in graphene are observed (orange arrows in A). At lower temperatures, ruptured regions where graphene did not adhere to Nafion well are seen from the flipped over regions near edges (purple arrows). (D) Analysis of defective area attributed to oxidation (orange bars) and ruptures (purple bars) shows a trade-off in defect types with a minima ~ 115 °C. Inset shows the DSC plots for as received and hot-pressed N211- H^+ form membrane. A dotted line shows the $T_{\text{opt}} \sim 115$ °C which is near the end of the glass transition region of N211 polymer. Schematics of the graphene|Nafion interface (E) $T > T_{\text{opt}}$, (F) $T \sim T_{\text{opt}}$ and (G) $T < T_{\text{opt}}$, where T_{opt} is the optimum temperature of hot-press. When $T > T_{\text{opt}}$, the Nafion conformally contacts the graphene surface. However, the high temperature tends to oxidize the Cu foil underneath defects in graphene (orange circles). At $T < T_{\text{opt}}$, the Nafion does not make conformal contact (white patches) resulting in regions of patchy graphene transfer. Upon etching the Cu foil, these poorly-adhered regions tend to delaminate from the Nafion and are seen as a patch next to the ruptured area, as shown in (C).



originate from non-conformal contact between the Nafion and the graphene/Cu surface (Fig. 3E–G). We note conformal contact between Nafion and graphene|Cu depends on the glass transition regime of Nafion. Hence, differential scanning calorimetry (DSC) studies were performed to understand the glass transition behaviour of Nafion (inset Fig. 3D).^{42–44} The onset of the glass transition regime is $\sim 60\text{--}70\text{ }^{\circ}\text{C}$, as indicated by the increased slope (inset Fig. 3D). The heat flow stabilizes at $\sim 125\text{ }^{\circ}\text{C}$, indicating the polymer has undergone a complete glass transition. This behaviour is similar to prior reports^{42–44} and attributed to the relaxation of the PTFE backbone of Nafion. The DSC curve yields a conventional glass transition temperature $T_g \sim 100\text{ }^{\circ}\text{C}$ (taken as the midpoint between the onset and stabilized temperatures). Similar behaviour is observed for the sample which was hot pressed for 45 s at $115\text{ }^{\circ}\text{C}$. The minor differences in onset temperature point and heat flow for the as received N211 and hot-pressed Nafion are attributed to slight differences in sample weight, minor water loss and increased crystallinity of Nafion possible from hot-press. Based on the glass transition features of N211 and the observed optimum transfer of graphene on Nafion, $T_{\text{opt}} \sim 115\text{ }^{\circ}\text{C}$ corresponds to near complete glass transition of Nafion, resulting in improved conformal contact between Nafion and graphene|Cu (Fig. 3F).^{42–44}

Above T_{opt} , conformal contact between Nafion and graphene on Cu is possible, but the higher temperature leads to oxidation of Cu underneath the graphene that results in damages with dark spots and line like features (Fig. 3E), that are similar to etch pits in Fig. 2 (also see Table 1). In order to reach an intermediate trade-off between these two defect types, we transferred graphene at $T_{\text{opt}} \sim 115\text{ }^{\circ}\text{C}$ and indeed observed a minimum occurrence of both defect types. The schematics of graphene|Nafion interfaces are shown in Fig. 3E–G for different hot-press temperatures to emphasize the conformal contact between Nafion and graphene as well as oxidation features on copper.

Finally, for a comprehensive evaluation of hot-press parameters, we rationalize the low-pressure during graphene transfer on Nafion *via* hot-press at optimum condition of $115\text{ }^{\circ}\text{C}$ (Fig. 3) and 45 s (Fig. 2). Fig. 4A and B show SEMs of graphene transferred at 200 psi and 1000 psi, respectively. An increase in ruptures in the graphene is observed at higher pressure which is likely due to combined effect of Cu metal deformation under load and compressibility of Nafion at high pressure (Fig. 4C and D).

Using the optimized transfer conditions, we fabricated a Nafion|graphene|Nafion (N211|G|N211) sandwich membrane and evaluate the efficacy of the PEM by measuring proton transport and hydrogen crossover, respectively using a custom-built set-up

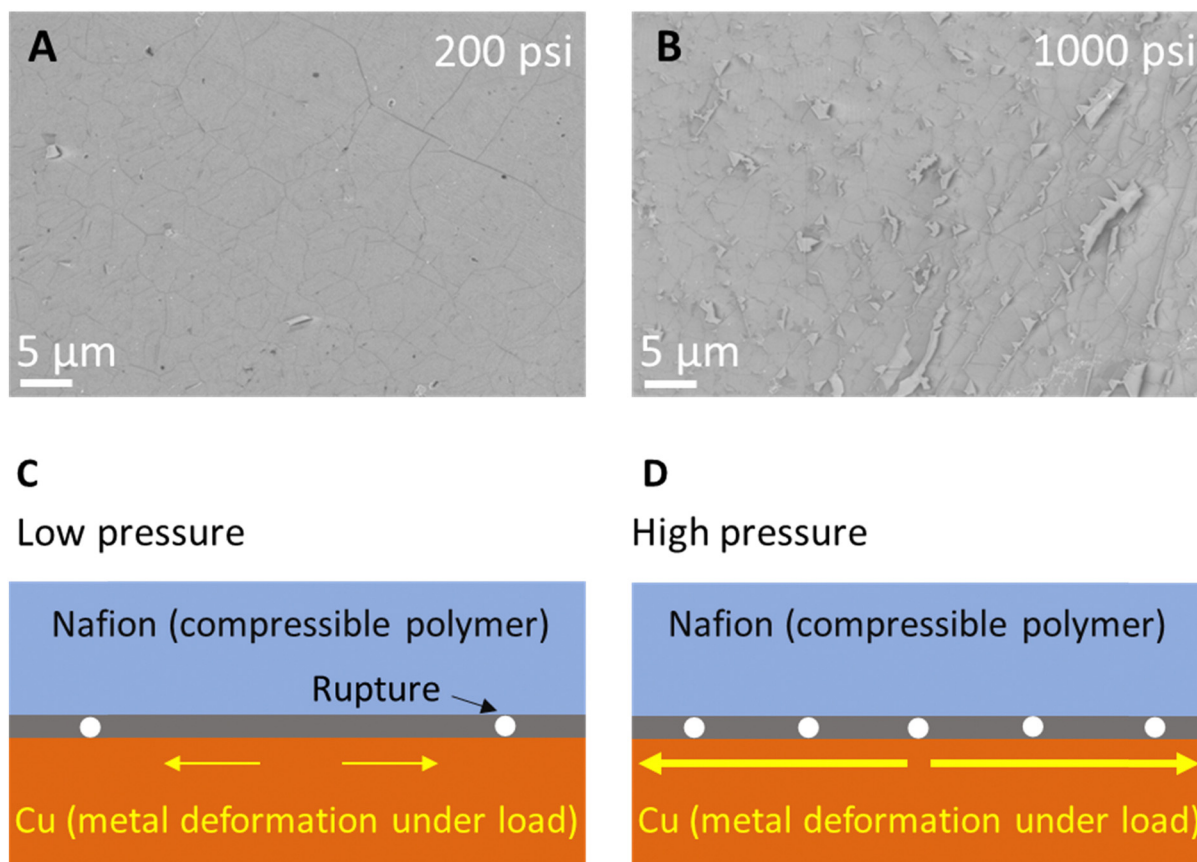


Fig. 4 Graphene transfer on Nafion at $115\text{ }^{\circ}\text{C}$, hot-pressed at pressures (A) 200 psi, (B) 1000 psi for 45 s. (C) and (D) At higher pressure the ruptures in the transferred graphene increase due to increase in metal deformation of the Cu foil (note Cu is a soft and malleable metal which is subject to deformation/elongation under pressure). Such metal deformation results in ruptures to the graphene on Cu (see schematics).



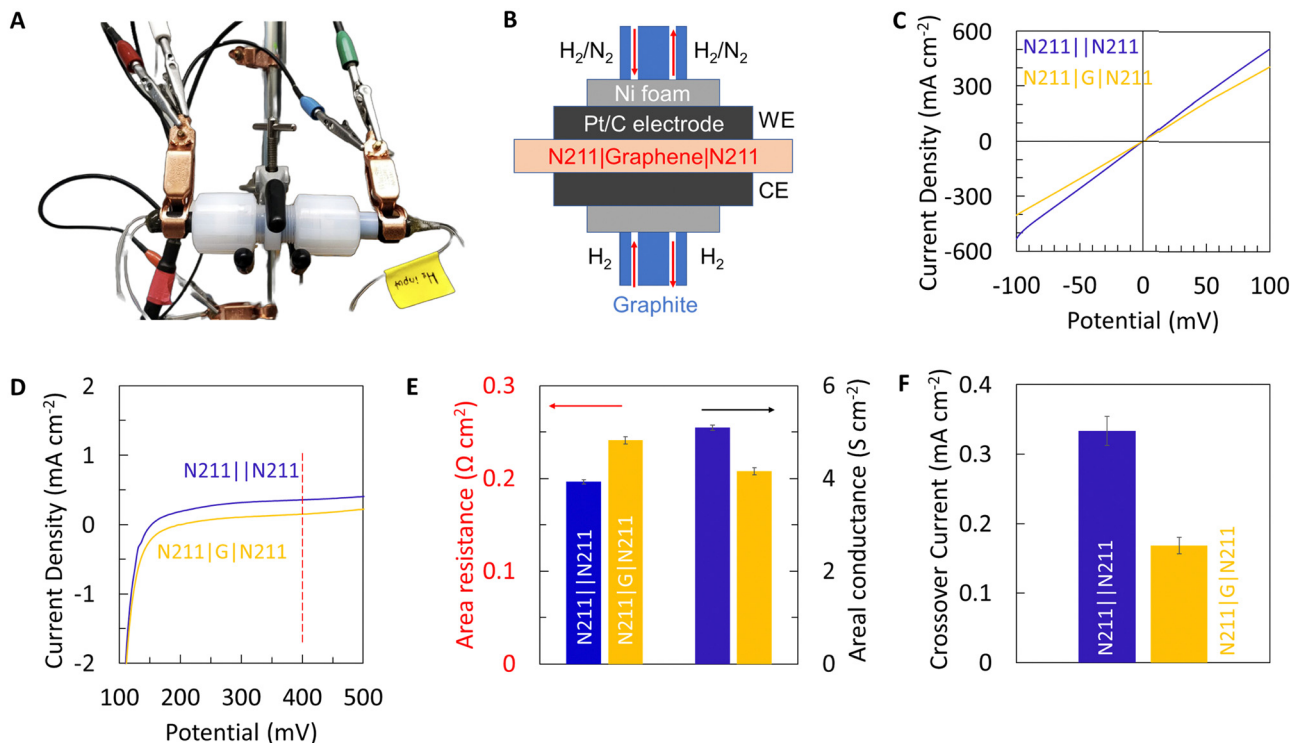


Fig. 5 Gas phase proton transport measurements for PEM membrane-electrode assembly (MEAs) prepared *via* hot-press at 115 °C, 200 psi and 45 s. (A) Custom-built experimental set-up, (B) schematic of the MEA, (C) *I*-*V* plots with symmetric gas feed *i.e.* H₂ gas on both sides of the MEA, (D) *I*-*V* plots exhibiting the hydrogen crossover current segment measured with H₂ on one side and N₂ gas feed on the other. (E) Area specific resistance (ASR) and areal conductance extracted from (C). (F) Crossover current density extracted from (D) at 0.4 V for N211||N211 control and N211|G|N211 membranes.

(Fig. 5A). A schematic of the electrical connections and the membrane electrode assembly is shown in Fig. 5B. Fig. 5C, presents the *I*-*V* curves (obtained by feeding humidified H₂ gas to both sides) for Nafion control membranes as well as N211|G|N211 sandwich membranes. The addition of graphene results in a marginal decrease in the measured current, indicating a marginal increase in the resistance (decrease in conductance) for protons (Fig. 5C and E). However, this marginal decrease in proton conductance with the addition of graphene is also accompanied by a substantial decrease in the hydrogen crossover current density (Fig. 5D). We note the transport mechanisms of protons and H₂ gas (crossover) are different in Nafion. H₂ transport primarily occurs in water channels in Nafion. Hence, an overlap of water channel pores in Nafion with macroscopic transfer defects in graphene will be necessary for H₂ crossover to occur.

The proton resistance for Nafion control and graphene sandwich membranes are extracted from the *I*-*V* plots (shown in Fig. 5C) using Ohm's law and normalized to the membrane area $\sim 0.32 \text{ cm}^2$ for area specific proton resistance (ASR). Fig. 5E, presents the area specific proton resistance for Nafion control membranes $\sim 0.19 \Omega \text{ cm}^2$ (areal conductance $\sim 5.1 \text{ S cm}^{-2}$) and graphene sandwich membranes $\sim 0.24 \Omega \text{ cm}^2$ (areal conductance $\sim 4.2 \text{ S cm}^{-2}$), respectively. Additionally, Fig. 5F shows the hydrogen crossover current (extracted from Fig. 5D) for Nafion control membranes ($\sim 0.33 \text{ mA cm}^{-2}$) and graphene sandwich membranes ($\sim 0.17 \text{ mA cm}^{-2}$) at 0.4 V at room temperature in a humidified environment. Notably, the

graphene sandwich membranes fabricated using the optimal transfer process reduces the hydrogen crossover by $\sim 50\%$, while still maintaining $\text{ASR} < 1 \Omega \text{ cm}^2$ (areal proton conductance $> 1 \text{ S cm}^{-2}$) adequate for enabling practical applications, thereby demonstrating the advantage of incorporating CVD graphene with Nafion for PEM applications.

Conclusions

To summarize, we systematically probed the influence of hot-press time, temperature and pressure for the direct transfer of CVD graphene onto Nafion. Our results indicate that hot-pressing for $\sim 120 \text{ s}$ results in increased dark spot features that correspond to oxidation of Cu underneath defects in graphene compared to shorter time duration $\sim 45 \text{ s}$. The temperature of hot-press and its interplay with the glass transition temperature region of Nafion has a significant influence on graphene transfer. The optimum hot-press temperature, $T_{\text{opt}} \sim 115 \text{ }^\circ\text{C}$ corresponds to near complete glass transformation of Nafion (glass transition temperature range $65\text{--}125 \text{ }^\circ\text{C}$, $T_g \sim 100 \text{ }^\circ\text{C}$). Transfers at $T < T_{\text{opt}}$ suffer from ruptures in graphene originating from lack of conformal contact between Nafion and graphene while $T > T_{\text{opt}}$ results in increased Cu oxidation related defects in graphene due to higher temperature. $T \sim T_{\text{opt}}$ results in a minima for both ruptures and oxidation related defects in graphene. Finally, higher hot-press pressures resulted in significantly higher



ruptures on graphene due to deformation of Cu, suggesting that low pressure is more suitable for graphene transfer on Nafion. Using the optimal transfer conditions, we fabricated Nafion|G|Nafion sandwich membranes that show ~50% reduction in hydrogen crossover ($\sim 0.17 \text{ mA cm}^{-2}$) in comparison to Nafion control membranes ($\sim 0.33 \text{ mA cm}^{-2}$) while maintaining adequate ASR $< 0.25 \text{ } \Omega \text{ cm}^2$ (areal conductance $\sim 4\text{--}5 \text{ S cm}^{-2}$) to enable practical PEM applications.

Author contributions

P. R. K. conceived and supervised the project. P. C., N. K. M., T. K., and R. S. performed the transfers, characterization, and analysed the results. P. C., N. K. M., and P. R. K. wrote the manuscript with input and revisions from all authors.

Conflicts of interest

P. R. K. acknowledges stake in a company aimed at commercializing 2D materials.

Acknowledgements

The use of Vanderbilt Institute of Nanoscale Science and Engineering CORE facilities are acknowledged. This work was supported in part by NSF CAREER award #1944134, in part by DOE Early Career Research Program award # DE-SC0022915, in part by the U.S. Department of Energy Isotope Program, managed by the Office of Science for Isotope R&D and Production under award number DE-SC0022237. P. R. K. acknowledges the ECS Toyota Young Investigator Award. Part of this work was performed at the Center for Nanophase Materials Sciences at Oak Ridge National Laboratory, a U.S. Department of Energy Office of Science User Facility. Authors appreciate and acknowledge assistance from Dr. Aaron Daniel at the Department of Chemistry at Vanderbilt University for Differential Scanning Calorimetry measurements.

Notes and references

- P. R. Kidambi, P. Chaturvedi and N. K. Moehring, *Science*, 2021, **374**, eabd7687, DOI: [10.1126/science.abd7687](https://doi.org/10.1126/science.abd7687).
- S. Bukola, Z. Li, J. Zack, C. Antunes, C. Korzeniewski, G. Teeter, J. Blackburn and B. Pivovar, *J. Energy Chem.*, 2021, **59**, 419–430.
- S. Hu, M. Lozada-Hidalgo, F. C. Wang, A. Mishchenko, F. Schedin, R. R. Nair, E. W. Hill, D. W. Boukhvalov, M. I. Katsnelson, R. A. W. Dryfe, I. V. Grigorieva, H. A. Wu and A. K. Geim, *Nature*, 2014, **516**, 227–230.
- J. S. Bunch, S. S. Verbridge, J. S. Alden, A. M. Van Der Zande, J. M. Parpia, H. G. Craighead and P. L. McEuen, *Nano Lett.*, 2008, **8**, 2458–2462.
- H. Qi, Z. Li, Y. Tao, W. Zhao, K. Lin, Z. Ni, C. Jin, Y. Zhang, K. Bi and Y. Chen, *Nanoscale*, 2018, **10**, 5350–5357.
- K. S. Novoselov, A. K. Geim, S. V. Morozov, D. Jiang, Y. Zhang, S. V. Dubonos, I. V. Grigorieva and A. A. Firsov, *Science*, 2004, **306**, 666–669.
- N. Metzger, I. Vlasiouk, S. Smirnov, G. Mariscal, R. Spragg and X. Li, *J. Electrochem. Energy Convers. Storage*, 2023, **20**(2), 020903.
- Q. Chen, Y. Y. Du, K. M. Li, H. F. Xiao, W. Wang and W. M. Zhang, *Mater. Des.*, 2017, **113**, 149–156.
- M. Lozada-Hidalgo, S. Zhang, S. Hu, A. Esfandiari, I. V. Grigorieva and A. K. Geim, *Nat. Commun.*, 2017, **8**, 15215.
- S. Bukola, Y. Liang, C. Korzeniewski, J. Harris and S. Creager, *J. Am. Chem. Soc.*, 2018, **140**, 1743–1752.
- X. H. Yan, R. Wu, J. B. Xu, Z. Luo and T. S. Zhao, *J. Power Sources*, 2016, **311**, 188–194.
- S. M. Holmes, P. Balakrishnan, V. S. Kalangi, X. Zhang, M. Lozada-Hidalgo, P. M. Ajayan and R. R. Nair, *Adv. Energy Mater.*, 2017, **7**, 1601216.
- P. Chaturvedi, I. V. Vlasiouk, D. A. Cullen, A. J. Rondinone, N. V. Lavrik and S. N. Smirnov, *ACS Nano*, 2019, **13**, 12109–12119.
- M. I. Walker, P. Braeuninger-Weimer, R. S. Weatherup, S. Hofmann and U. F. Keyser, *Appl. Phys. Lett.*, 2015, **107**, 213104.
- J. L. Achtyl, R. R. Unocic, L. Xu, Y. Cai, M. Raju, W. Zhang, R. L. Sacci, I. V. Vlasiouk, P. F. Fulvio, P. Ganesh, D. J. Wesolowski, S. Dai, A. C. T. Van Duin, M. Neurock and F. M. Geiger, *Nat. Commun.*, 2015, **6**, 1–7.
- P. Chaturvedi, N. K. Moehring, P. Cheng, I. Vlasiouk, M. S. H. Boutilier and P. R. Kidambi, *J. Mater. Chem. A*, 2022, **10**, 19797–19810.
- S. Bukola, K. Beard, C. Korzeniewski, J. M. Harris and S. E. Creager, *ACS Appl. Nano Mater.*, 2019, **2**, 964–974.
- N. K. Moehring, P. Chaturvedi, P. Cheng, W. Ko, A. P. Li, M. S. H. Boutilier and P. R. Kidambi, *ACS Nano*, 2022, **16**, 16003–16018.
- P. R. Kidambi, G. D. Nguyen, S. Zhang, Q. Chen, J. Kong, J. Warner, A. P. Li and R. Karnik, *Adv. Mater.*, 2018, **30**, 1804977.
- P. Cheng, F. Fornasiero, M. L. Jue, W. Ko, A. P. Li, J. C. Idrobo, M. S. H. Boutilier and P. R. Kidambi, *Nat. Commun.*, 2022, **13**, 1–12.
- P. Cheng, M. M. Kelly, N. K. Moehring, W. Ko, A.-P. Li, J. C. Idrobo, M. S. H. Boutilier and P. R. Kidambi, *Nano Lett.*, 2020, **20**, 5951–5959.
- S. Bukola and S. E. Creager, *ECS Trans.*, 2019, **92**, 439–444.
- L. G. P. Martins, Y. Song, T. Zeng, M. S. Dresselhaus, J. Kong and P. T. Araujo, *Proc. Natl. Acad. Sci. U. S. A.*, 2013, **110**, 17762–17767.
- S. Bae, H. Kim, Y. Lee, X. Xu, J.-S. Park, Y. Zheng, J. Balakrishnan, T. Lei, H. Ri Kim, Y. Il Song, Y.-J. Kim, K. S. Kim, B. Özyilmaz, J.-H. Ahn, B. H. Hong and S. Iijima, *Nat. Nanotechnol.*, 2010, **5**, 574–578.
- S. J. Osborn, M. K. Hassan, G. M. Divoux, D. W. Rhoades, K. A. Mauritz and R. B. Moore, *Macromolecules*, 2007, **40**, 3886–3890.
- G. Calleja, A. Jourdan, B. Ameduri and J. P. Habas, *Eur. Polym. J.*, 2013, **49**, 2214–2222.



- 27 S. Yasuda, H. Matsushima, K. Harada, R. Tanii, T. O. Terasawa, M. Yano, H. Asaoka, J. S. Gueriba, W. A. Diño and K. Fukutani, *ACS Nano*, 2022, **16**, 14362–14369.
- 28 S. M. Andersen, R. Dhiman, M. J. Larsen and E. Skou, *Appl. Catal., B*, 2015, **172–173**, 82–90.
- 29 X. Wang, Y. Zhang, Y. Zhu, S. Lv, H. Ni, Y. Deng and Y. Yuan, *Membranes*, 2022, **12**, 431.
- 30 I. Vlassioug, M. Regmi, P. Fulvio, S. Dai, P. Datskos, G. Eres and S. Smirnov, *ACS Nano*, American Chemical Society, 2011, vol. 5, pp. 6069–6076.
- 31 I. Vlassioug, P. Fulvio, H. Meyer, N. Lavrik, S. Dai, P. Datskos and S. Smirnov, *Carbon*, 2013, **54**, 58–67.
- 32 S. Dhingra, J.-F. Hsu, I. Vlassioug and B. D'Urso, *Carbon*, 2014, **69**, 188–193.
- 33 P. R. Kidambi, C. Ducati, B. Dlubak, D. Gardiner, R. S. Weatherup, M. B. Martin, P. Seneor, H. Coles and S. Hofmann, *J. Phys. Chem. C*, 2012, **116**, 22492–22501.
- 34 P. Cheng, J. Espano, A. Harkaway, A. E. Naclerio, N. K. Moehring, P. Braeuninger-Weimer and P. R. Kidambi, *ACS Appl. Mater. Interfaces*, 2022, **14**, 41328–41336.
- 35 P. R. Kidambi, D. Jang, J. C. Idrobo, M. S. H. Boutilier, L. Wang, J. Kong and R. Karnik, *Adv. Mater.*, 2017, **29**, 1700277.
- 36 P. Cheng, N. K. Moehring, J. C. Idrobo, I. N. Ivanov and P. R. Kidambi, *Nanoscale*, 2021, **13**, 2825–2837.
- 37 P. R. Kidambi, R. A. Terry, L. Wang, M. S. H. Boutilier, D. Jang, J. Kong and R. Karnik, *Nanoscale*, 2017, **9**, 8496–8507.
- 38 C. A. Schneider, W. S. Rasband and K. W. Eliceiri, *Nat. Methods*, 2012, **9**, 671–675.
- 39 X. Xue, X. Chu, M. Zhang, F. Wei, C. Liang, J. Liang, J. Li, W. Cheng, K. Deng and W. Liu, *ACS Appl. Mater. Interfaces*, 2022, **14**, 32360–32368.
- 40 A. Das, B. Chakraborty and A. K. Sood, *Bull. Mater. Sci.*, 2008, **31**, 579–584.
- 41 A. C. Ferrari and D. M. Basko, *Nat. Nanotechnol.*, 2013, **8**, 235–246.
- 42 S. H. De Almeida and Y. Kawano, *J. Therm. Anal. Calorim.*, 1999, **58**, 569–577.
- 43 Y. S. Kim, L. Dong, M. A. Hickner, T. E. Glass, V. Webb and J. E. McGrath, *Macromolecules*, 2003, **36**, 6281–6285.
- 44 H. Y. Jung and J. W. Kim, *Int. J. Hydrogen Energy*, 2012, **37**, 12580–12585.

